An experimental and numerical case study of thermal and mechanical consequences induced by laser welding process

Yabo Jia, Yassine Saadlaoui, H. Hamdi, Julien Sijobert, Jean-Christophe Roux, Jean-Michel Bergheau

Case Studies in Thermal Engineering 35 (2022) 102078

Contents lists available at ScienceDirect

Case Studies in Thermal Engineering

journal homepage: www.elsevier.com/locate/csite

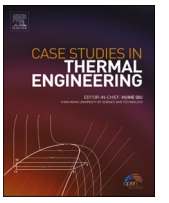

An experimental and numerical case study of thermal and mechanical consequences induced by laser welding process

Yabo Jia *, Yassine Saadlaoui, Hédi Hamdi, Julien Sijobert, Jean-Christophe Roux, Jean-Michel Bergheau

University of Lyon, Ecole Centrale de Lyon-ENISE, LTDS, UMR 5513 CNRS, 58 rue Jean Parot, 42023, Saint-Etienne Cedex 02, France

ARTICLE INFO

Keywords:
Experimental benchmark
Laser welding process
Finite element method
Thermo-mechanical simulation

ABSTRACT

In this study, an experimental benchmark with different welding conditions is developed. In-situ diagnostics tools (high-speed camera, thermocouple) and ex-situ diagnostics devices (high-resolution digital microscope, measuring arm, X-Ray diffraction device) are exploited to measure various physical quantities. These measurements set up a complete database of laser welding benchmarks, which can establish a relationship between welding parameters and thermo-mechanical consequences. Meanwhile, the finite element method is used to investigate such a process and understand the multi-physics coupling problems behind the process. Numerical and experimental comparisons are performed in two steps. Firstly, the molten pool morphology and temperature evolution are employed to calibrate the 3D volumetric heat source. Secondly, a thermo-mechanical coupling is carried out by imposing the thermal strain calculated from the calibrated thermal model. Thermo-elastoplastic models with isotropic and kinematic hardening are used to compute the distortion and residual stresses. Mechanical results (distortions and residual stresses) of numerical models are compared with those of the benchmark. Overall, a good correlation is found. Thus, this paper provides a full experimental case study and numerical solution for laser welding process, which allows researchers to validate their numerical models and also gives some insights for modeling welding processes.

Nomenclature

X	coordinate perpendicular to scanning direction (mm)
Y	coordinate along scanning direction (mm)
Z	coordinate in depth (m)
C	heat capacity (J/K)
T	temperature (K)
$\alpha^T(T)$	thermal expansion coefficient ($1/K$)
q_{heat}	input heat flux (W)
q_{loss}	heat losses (W)
$Re2$	heat source parameters (mm)
$Ri2$	heat source parameters (mm)

* Corresponding author.
E-mail address: yabo.jia@enise.fr (Y. Jia).

https://doi.org/10.1016/j.csite.2022.102078
Received 8 February 2022; Received in revised form 20 April 2022; Accepted 28 April 2022
Available online 6 May 2022

$Ratio$	heat source parameters (mm)
n	heat source parameters ($-$)
T_{air}	room temperature (K)
H_1	kinematic parameters (Pa)
H_2	kinematic parameters (Pa)
Q_0	normalized maximal energy input (W/mm^3)
h_{con}	convective loss coefficient (W/mm^2K)
λ_{ii}	thermal conductivity in ii direction ($W/mm\ K$)
ρ	material density (Kg/mm^3)
ε	surface emissivity (0.8)
δ	Stefan-Boltzmann constant ($Kg/s^{-3}K^{-4}$)
$\boldsymbol{\sigma}$	cauchy stress (Pa)
$\boldsymbol{S}$	fourth-order compliance (Pa)
$\overrightarrow{f}$	body force (N/mm^3)
$\overrightarrow{u}$	displacement (mm)
$\boldsymbol{\epsilon}$	linearized strain ($-$)
$\boldsymbol{\epsilon^e}$	elastic strain ($-$)
$\boldsymbol{\epsilon^p}$	plastic strain ($-$)
$\boldsymbol{\epsilon^T}$	thermal strain ($-$)
γ_1	kinematic parameters ($-$)
σ_Y	yield stress (Pa)

1. Introduction

Laser welding process is widely used in the industry for joining high integrity components. The heat source generated by laser beam impacts directly the size of the melting and heat-affected zones. Distortions induced by high power density welding technologies (laser welding, electron-beam welding) are generally less than those of other classical welding technologies (arc welding, resistance welding, etc.). Moreover, high welding speed, well-controlled welding path, welding without contact, and possibilities of assembling different materials (both metallic and non-metallic) are its main advantages. All these features make laser welding technology becoming an increasing process. Apart from welding [1,2], laser can also be used for various materials processing applications, such as heat treatment [3], selective laser melting [4] and surfacing [5], etc.

The wide use of laser welding process and the need to improve its performance led to the development of several studies. Experimental approach is often used to study and analyze this thermo-mechanical process. For example, Rong et al. [6] have studied the phase transformation during the laser welding of EH36. Xu et al. [7] and Deraskhshan et al. [8] have investigated the residual stress of butt joint induced by laser welding. Ramkumara et al. [9] and Saadlaoui et al. [10] have worked on the microstructure and melt pool morphology. Generally, it consists in optimizing the process parameters, such as laser power distribution [11], laser welding condition [12–14], to ensure a better quality of welded parts. However, experimental trials are not always accessible and they can be very expensive considering that the process parameters are numerous. For these reasons, numerical simulation is of special interest for optimizing process parameters, and for predicting the final consequence of welded parts with a reasonable cost and computation time.

Numerical approaches used to simulate the laser welding can be classified into two groups according to the modeling scale. The first group includes the thermo-mechanical simulation to predict the mechanical consequences (distortions and residual stresses) induced by welding. For example, Ahn et al. [15] and Chen et al. [16] have studied residual stresses in laser welded T-joints. These stresses in multipass welding have been modeled by Duranton et al. [17] and Feulvarch et al. [18]. Herrnring et al. [19] have investigated the residual stresses considering the precipitation. Huang et al. [20,21] proposed high efficient finite element models based on local mesh refining method and Graphics Processing Unit for predicting residual stress. The second group consists in simulating the process itself (multi-physics simulation) considering the fluid flow in the weld pool. For example, Saadlaoui et al. [22] and Zhang et al. [23] have studied the effect of fluid flow on simulation accuracy of the thermal field. The laser welding on key-hole has been simulated by Xu et al. [24] and Xie et al. [25]. Jiang et al. [26] have studied the effect of fluid flow on solidification. Compared to the multi-physics simulations, thermo-mechanical simulations are widely used because of their lower computation cost. Moreover, the thermo-mechanical simulations allow estimating residual stresses and distortions at the same scale as industrial structures, thus providing very useful information for fatigue lifetime predictions or welding sequence optimization. However, thermo-mechanical models require calibration of heat source and must be validated by comparing numerical results (melt pool morphology, thermal cycles, residual distortions, etc.) with those of experimental tests.

Different experimental measurements have been reported in the literature to satisfy the numerous research demands in laser welding. For example, Lei et al. [1] measured the deformation of cutting surface to validate their mechanical model. Similarly, to investigate the inhomogeneity of AISI 316L butt joint part, Rong et al. [2,6,7] measured the melt pool morphology and angular distortion after the welding process for validating their numerical models. Gao et al. [27] studied the formation of molten pool and the keyhole during Nd: YAG laser welding of stainless steel. Derakhshan et al. [8] only employed the ex-situ diagnostics tools to investigate

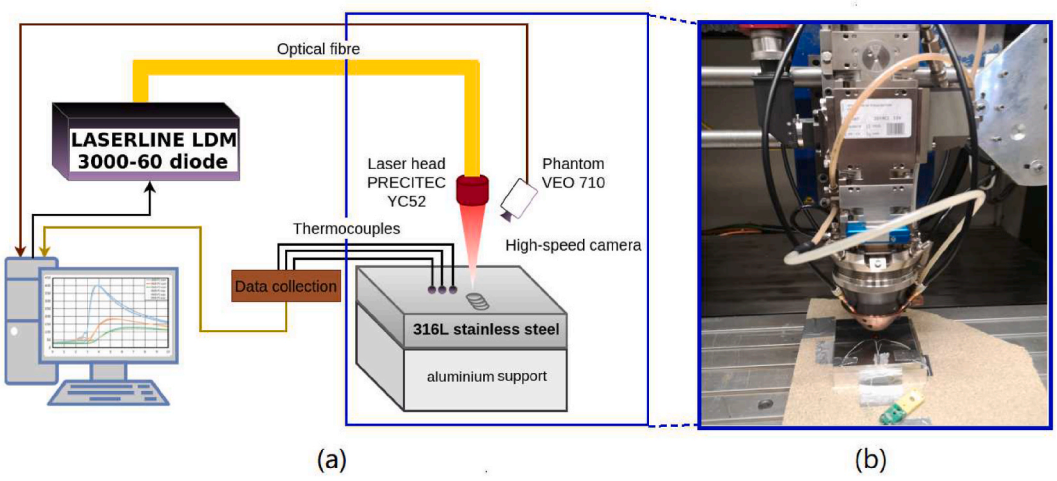

Fig. 1. (a) Diagram of experiment setup and (b) machine laser head.

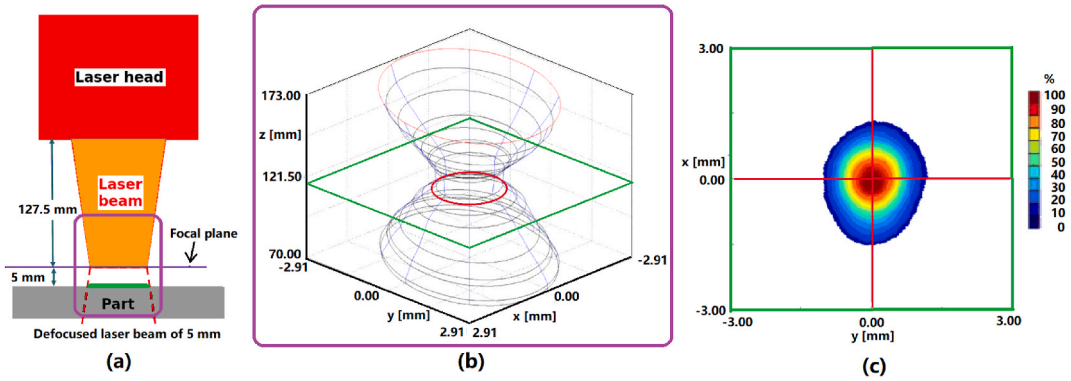

Fig. 2. (a) Diagram of defocused laser beam; (b) laser beam analysis; (c) energy distribution of defocused laser beam.

residual stress and welding distortion induced by laser-based welding processes, which cannot provide the information during the processes. Ramkumar et al. [9] provided only melt pool shape after the laser welding process. Performing a complete experimental benchmark is quite complex, and requires the installation of various in-situ and ex-situ diagnostics tools. Different physical quantities were measured separately by the aforementioned work. However, a complete experimental benchmark that allows validating different models, in both thermal and mechanical aspects, is still lacking.

In this context, a complete benchmark, including melt pool morphology, temperature evolution, distortion, and residual stress, is presented. To benefit the developed experimental benchmark and study the laser welding process, a thermo-mechanical simulation is also presented in this paper. This benchmark allows calibrating and validating the thermo-mechanical model, and the numerical model can provide supplementary details and results on the laser welding process.

The paper is organized as follows:

- The proposed experimental set-up is presented in Section 2;
- Some details of numerical model are presented in Section 3,
- Numerical and experimental results are compared and discussed in Section 4.
- Conclusions are addressed in Section 5.

2. Experimental set-up

As it is shown in Fig. 1, a specific experimental setup is designed and carried out by using two in-situ diagnostics tools (high-speed camera, thermocouples). These tools allow us to capture the evolution of temperature and molten pool morphology during the laser welding process.

A TRUMP LASMA 1054 CNC machine, a PRECITEC YC52 laser head, and a LASERLINE LDM 3000-60 diode multimode laser source (with a power of 3 kW and a wavelength of 930 nm) is used in this study. This multimode laser is generally used only for conduction mode manufacturing processes (welding, selective laser melting, laser cladding, etc). A real laser power of 2.5 kW was measured by a

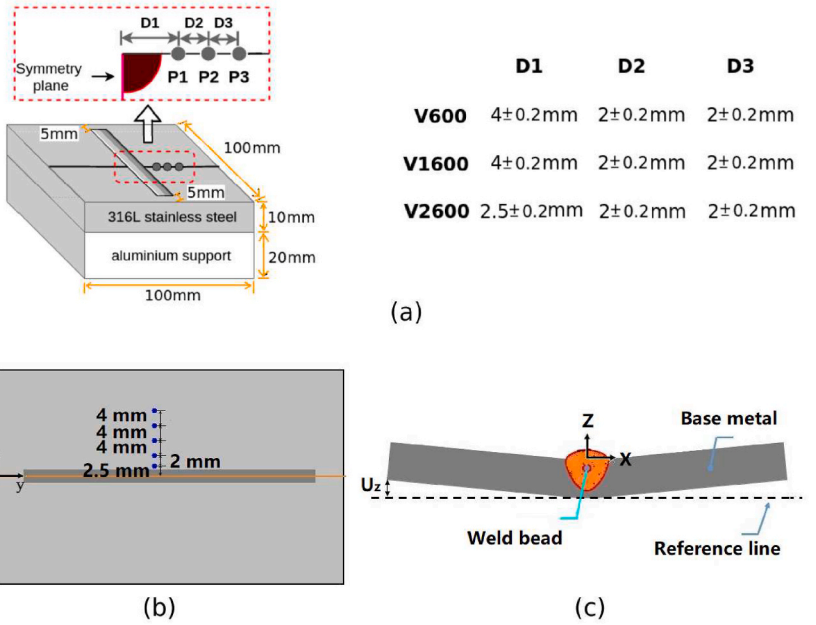

	D1	D2	D3
V600	4±0.2mm	2±0.2mm	2±0.2mm
V1600	4±0.2mm	2±0.2mm	2±0.2mm
V2600	2.5±0.2mm	2±0.2mm	2±0.2mm

Fig. 3. Weld's sketch: (a) Locations of thermocouples; (b) Positions for where residual stress are determined; (c) x-z cross section in the middle of weld's length: measurements of maximum vertical displacement Uz.

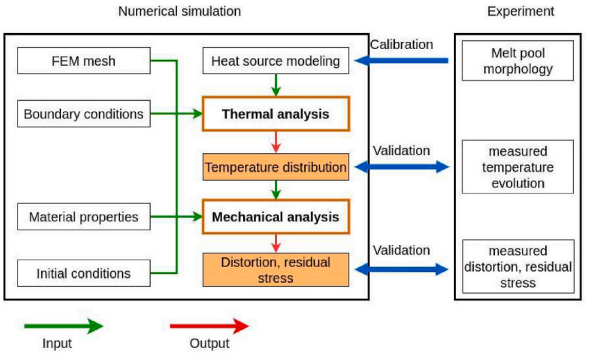

Fig. 4. Thermo-mechanical simulations procedure and couplings with experiments.

wattmeter. Laser beam is defocused by 5 mm to carry out a laser welding by conduction (without keyhole). This configuration gives a laser beam diameter of 2.4 mm (Fig. 2). Samples 100 mm × 100 mm × 10 mm were extracted from an Austenite AISI 316L hot rolled plates. All samples were subjected to a relaxation heat treatment (610 $^{\circ}C$ for 2.5 h with slow natural cooling rate in a neutral atmosphere) to reduce residual stresses related to the machining and rolling processes. A single weld bead of 90 mm length is created for each sample. In order to have significant outputs for each experiment, three welding speeds of 600, 1600, and 2600 mm min^{-1} were tested and three samples are prepared for each welding speed.

A PHANTOM VEO 710 high-speed camera (resolution of 1280 × 800 pixels, maximal rate of 7400 *fps*) synchronized with an auxiliary laser light (CAVILUX diode laser) is used to track the formation of the weld pool. This system allows measuring the length and width of the weld pool. Its depth and height can be determined by observing a cross section with an optical microscope. Thermocouples of type K with a diameter of 0.2 mm are used to acquire temperature evolution.

A FARO GAGE 3D measuring arm with a precision of 0.02 mm is employed to measure maximal distortions induced by the welding. A *PROTO*^{TM} XRD device specially designed for residual stress determination is used to measure surface residual stresses. For each point, measurements in x and y-directions are carried out. A Manganese tube generating an X-Ray beam with a wavelength of about 2.10314 μm is chosen to make sure that the (*hkl*) Miller indices describing planes 311 of the stainless-steel FCC Crystallographic structure diffracted at the Bragg's angle 152.8°. The $sin^2(\psi)$ method is used to determine residual stress with X-ray elastic constants of the family of planes 311: $\frac{1}{2}S_{2311} = 7.18 \times 10^{-6}[MPa]^{-1}$ and $-S_{1331} = 1.20 \times 10^{-6}[MPa]^{-1}$. In the present study, fourteen ψ directions were considered.

Fig. 3 resumes the locations of thermocouples (P1,P2,P3), positions for measuring residual stress, and measurement of distortions

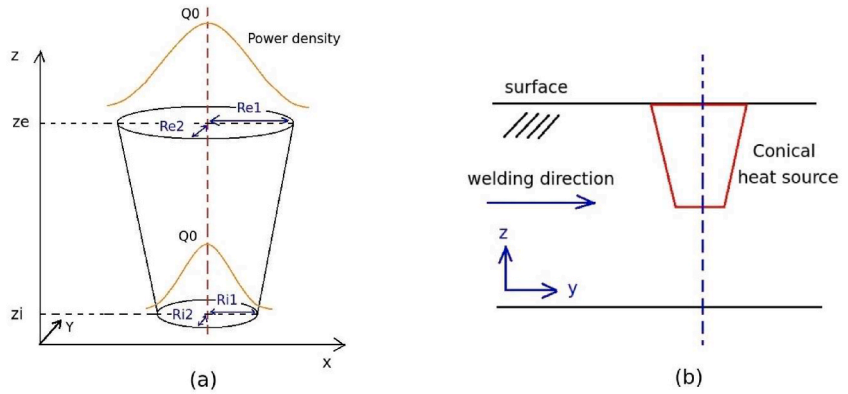

Fig. 5. Volumetric heat source: Power density distribution of the heat source on the top surface (a); Heat source position in the welding part, beneath the surface (b).

for different welding speed (600 mm/min, 1600 mm/min, 2600 mm/min).

3. Numerical model

In general, thermo-mechanical computation can be achieved in two steps: a strong coupled thermal and metallurgical simulation, followed by a mechanical computation taking into account temperature and metallurgical phases previously computed. In the present work, metallurgical transformations are disregarded; the application presented is the AISI 316L stainless steel devoid of such transformations. Fig. 4 resumes the numerical simulations procedure and the couplings with experimental benchmark. Experimental measurements can be used to calibrate and validate the numerical models, and the numerical results can enrich the database.

3.1. Thermal analysis

In the present study, thermal analysis is performed using classical first-order tetrahedral elements. Compared to hexahedral mesh, tetrahedral mesh can greatly facilitate the meshing of complex geometries using currently available meshing tools. In this section, thermal modeling is performed for simulating a moving heat source. In a solid medium with a domain Ω, governing equation for transient heat transfer analysis [28] is given by Eq. 1:

$$\begin{aligned} &\rho C\frac{\partial \mathrm{T}}{\partial \mathrm{t}} = \frac{\partial}{\partial \mathrm{x}}\left(\lambda_{\mathrm{xx}}\frac{\partial \mathrm{T}}{\partial \mathrm{x}}\right) + \frac{\partial}{\partial \mathrm{y}}\left(\lambda_{\mathrm{yy}}\frac{\partial \mathrm{T}}{\partial \mathrm{y}}\right) + \frac{\partial}{\partial \mathrm{z}}\left(\lambda_{\mathrm{zz}}\frac{\partial \mathrm{T}}{\partial \mathrm{z}}\right) + \mathrm{q}_{\mathrm{heat}} + \mathrm{q}_{\mathrm{loss}} \\ &\text{Fourier type condition: } \lambda \mathrm{grad}\, T \cdot \mathbf{n} = q(T,t) \quad \text{on } \partial\Omega_q \\ &\text{Dirichlet conditions: } T = T_p(t) \quad \text{on } \partial\Omega_T \\ &\partial\Omega = \partial\Omega_q \cup \partial\Omega_T \end{aligned} \tag{1}$$

where ρ, λ and C are, respectively, the density, conductivity and specific heat. $\lambda_{xx,yy,zz}$ represent the thermal conductivity of X,Y,Z direction. T is the temperature at nodes. $\partial\Omega$ is the boundary of domain Ω. q_{heat} represents the input heat flux to simulate the laser impact, and q_{loss} is the heat losses due to convection and radiation on the free surface.

As the fluid flow is neglected by Eq. 1, the thermal convection in the melt pool is missing. Therefore, different numerical models (without fluid flow) giving accurate prediction on the melt pool morphology have been proposed [29–31], which are based on a volumetric heat source or equivalent thermal conductivity technique. This paper adopts a volumetric heat source to simulate thermal convection in the melt pool.

An elliptical truncated conical shape heat source with Gaussian power density distribution (Q_0, Re1, Re2, Ratio, zi, ze) is proposed to simulate the laser impact. Fig. 5 shows the power density distribution of the proposed heat source and its position in the workpiece. Note that this heat source moves in Y direction. Its energy distribution is defined in Eq. (2):

$$\begin{aligned} q_{heat} &= n * \int Q_0 * \exp\left(-\frac{X^2}{a^2} - \frac{Y^2}{b^2}\right) \\ b &= \frac{Z - zi}{ze - zi} * (Re2 - Ri2) + Ri2 \\ a &= \frac{b}{\mathrm{Ratio}} \end{aligned} \tag{2}$$

The volumetric power density given by Eq. (2) is applied at the Gauss points. The total power really input in the model may therefore depends on the local mesh where the heat source applies. Therefore, the n value is calculated at each moment in order to ensure that the total power input is equal to desired value for the geometry considered.

Convective heat loss ($h_{con} = 20$ W/m^2) is computed by applying Newton's law:

Table 1
Parameters of Armstrong-Frederick model at different temperatures.

Temperature (°C)	γ_1	H_1	H_2	σ_y
20	90	4000	1635	260
200	85	3500	1517.5	173
400	55	2000	1285	140
500	40	800	1191.5	130
700	30	500	830	112
900	20	300	530	78
1000	5	20	385	57
1100	5	20	228	40
1400	60	120	1	1

$$q_{con} = h_{con}(T - T_{air}) \tag{3}$$

Heat dissipation by radiation is defiend by Stefan-Boltzmann's law:

$$q_{rad} = \delta\varepsilon(T^4 - T_{air}^4) \tag{4}$$

where δ, ε are Stefan-Boltzmann constant and the surface emissivity ($\varepsilon = 0.8$), respectively. T and T_{air} are in Kelvin.

3.2. Mechanical analysis

Regarding mechanical calculation, first-order tetrahedral finite elements are known to exhibit poor behavior in elastoplastic calculations based on von Mises plasticity criterion due to volumetric locking problems. The Nodal-Integration Based Finite Element Method (NI-FEM) presented in Jia et al. [32] is therefore used. The NI-FEM has been validated on different non-linear problems, including thermomechanical problems such as spot welding [33].

In the context of NI-FEM, the nodes are used as the integration points. Nodal strains are thus calculated as the mean values of the strains on the nodal domains. The stresses and the internal variables are then calculated at each node from the strain history by solving the constitutive equations of the material.

Now, let us first shortly review the equilibrium equation, dynamic effects being disregarded:

$$\overrightarrow{div}\boldsymbol{\sigma} + \overrightarrow{f} = \overrightarrow{0} \tag{5}$$

The global strain $\boldsymbol{\epsilon} = \frac{1}{2}\left(\mathbf{grad}\,\overrightarrow{u} + \mathbf{grad}^T\overrightarrow{u}\right)$ is the virtual linearized strain associated to the nodal displacement $\overrightarrow{u}$. This global strain can be decomposed as an elastic strain $\boldsymbol{\epsilon^e}$, a (visco)plastic strain $\boldsymbol{\epsilon^p}$, and a thermal strain $\boldsymbol{\epsilon^T}$.

Elastic strain, $\boldsymbol{\epsilon^e}$, is a function of the variation of stress tensor between the initial state ($\boldsymbol{\sigma_i}$) and actual state ($\boldsymbol{\sigma}$), which can be expressed as follow:

$$\boldsymbol{\epsilon^e} = \mathbf{S} : (\boldsymbol{\sigma} - \boldsymbol{\sigma}_i) \tag{6}$$

where $\mathbf{S}$ is the fourth-order compliance tensor defined by elastic coefficients.

Thermal strain, $\boldsymbol{\epsilon^T}$, depends on actual temperature T, reference temperature T_0 and expansion coefficient $\alpha^T(T)$, which can be written with the identity tensor $\boldsymbol{I}$ as follow:

$$\boldsymbol{\epsilon}^T = \alpha^T(T)(T - T_0)\boldsymbol{I} \tag{7}$$

The computation of plastic strain $\boldsymbol{\epsilon^p}$ is defined by three properties: (i) criterion for plasticity; (ii) flow rule; (iii) hardening model. In the case of laser welding, the criterion of von Mises is adopted, and metallic plastic behavior follows J_2 flow (2nd stress deviator tensor invariant) in general. In present study, the effect of hardening model is investigated and presented in the following part.

To descibe the material behavior of AISI 316L stainless steel during welding process, both isotropic and kinematic hardening model have been discussed and tested for predicting residual stress in multi-passe TIG welding [34]. Two hardening models perform in the same way for the first traction. However, once the material is plastically deformed, the isotropic hardening model will expand the elasticity domain, which means an increase of the yield strength. In the contrast, the kinematic hardening model will displace the center of the elastic domain. Kinematic strain-hardening model is always used to represent the Bauschinger effect, and are consequently recommended for cyclic loading.

In the context of laser welding process, one should know that the weld material undergoes a cyclic loading. Thus, the Bauschinger effect can be produced due to this cyclic load (especially for multi-passes case), and Depradeux et al. [35] shows the isotropic hardening would over-estimate the residual stresses. Therefore, it can be interesting to also test the kinematic hardening for welding simulations.

The uni-axial isotropic non-linear plastic strain-hardening curves of AISI 316L are taken from *SYSWELD*^{TM} database [36]. For kinematic hardening, the parameters of Armstrong-Frederick model have been calibrated to reproduce the same strain-stress curve at different temperatures (more details can be found in the documentation of *SYSWELD*^{TM} [36]), and the parameters are shown in Table 1. In the case of the material behavior must be characterized on the interval of important plastic strain, 3 linear kinematic variables have been considered. Then, the relationship between uni-axial strain and stress for the first tensile can be given by Eq. (8):

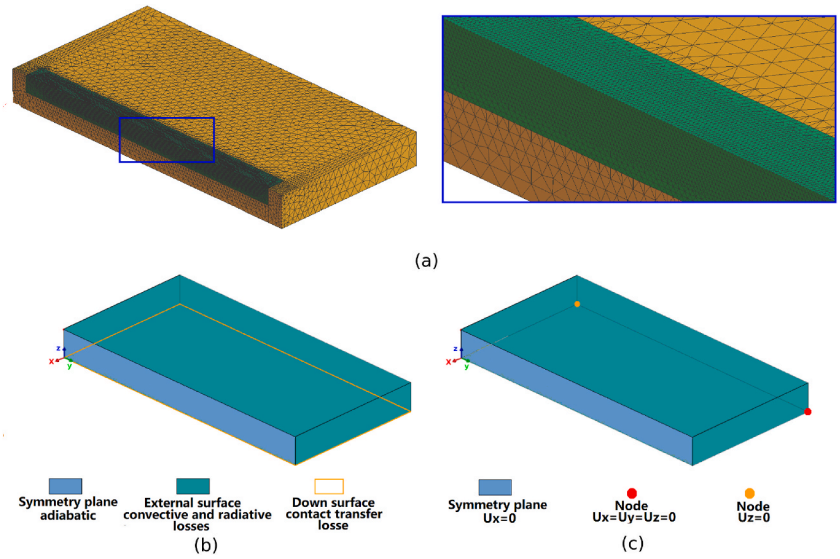

Fig. 6. Mesh and boundary conditions: (a) Free tetrahedral mesh (68,640 nodes/360,275 tetrahedrons); (b) thermal boundary conditions; (c) mechanical boundary conditions.

Table 2
Heat source parameters.

welding speed	Energy input	Q0	Re2	Ri2	Ratio	height (ze-zi)
600 mm/min	625	6	1.5	1.5	0.54	2.78
1600 mm/min	625	12	1.1	1.0	0.52	1.45
2600 mm/min	625	13	0.7	0.55	0.45	1.05

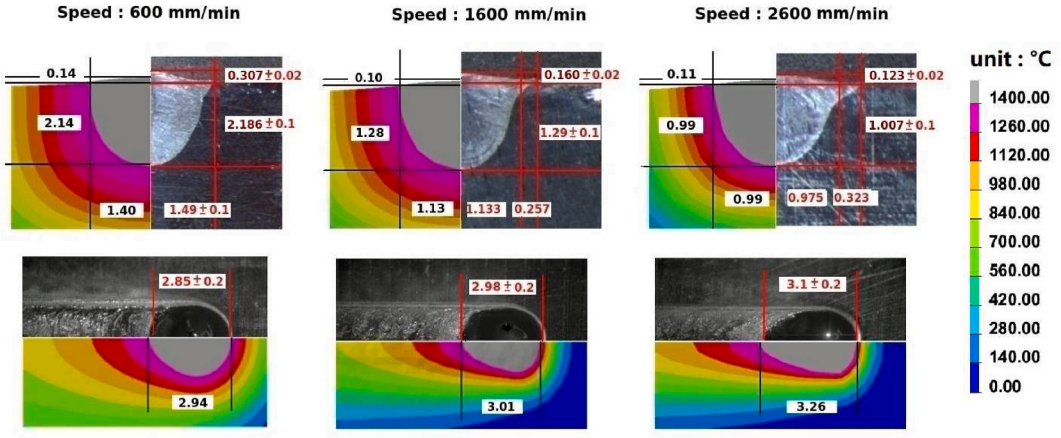

Fig. 7. Numerical and experimental results of the weld pool morphology (unit: mm).

$$\sigma = \frac{H_1}{\gamma_1}\left(1 - e^{(-\gamma_1 * \epsilon^p)}\right) + H_2 * \epsilon^p + \sigma_Y \tag{8}$$

where H_1, γ_1, H_2 are kinematic parameters to calibrate at different temperature and σ_Y is the yield stress.

3.3. Mesh, material properties and boundary conditions

The thermal physical properties of AISI 316L are equally taken from *SYSWELD*^{TM} database [36].

Fig. 6-(a) shows the FEM mesh for modeling laser welding process. Thanks to the symmetry plane, only half of the geometry needs to be discretized. The mesh is used for step-by-step transient simulation. Therefore, mesh must be refined along the heat source's trajectory.

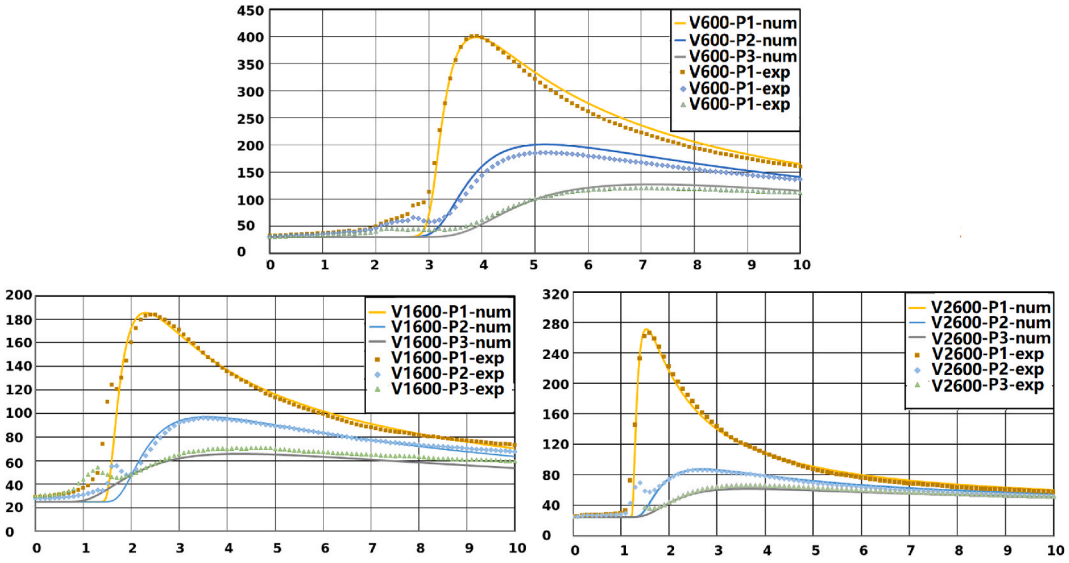

Fig. 8. Numerical and experimental results of the temperature evolution.

Table 3
Comparison of vertical displacements given by experimental measurements and simulations.

values/welding speed	V600	V1600	V2600
Measurements	0.411 ± 0.02	0.174 ± 0.02	0.091 ± 0.02
Isotropic-hardening	0.47	0.170	0.093
Kinematic-hardening	0.401	0.162	0.090

Fig. 6-(b)/(c) presents the boundary conditions for thermal analysis and mechanical analysis. Because of strong diffusivity of heat in the support made by 7020 aluminium alloy, the heat losses due to contact is considered. The aluminum support is simplified by a strong convective loss with the air, this heat transfer coefficient is calculated by using aluminum's thermal conductivity dividing by the thickness of aluminum support (0.136 $W/(mm*K)/20$ mm). A constant room temperature of 25 $^{\circ}C$ is considered for the aluminum support during the simulations. Mechanical contact with the aluminum support is out of considering since the plate is out constrained.

4. Results and discussion

The heat source parameters are calibrated by comparing the weld pool given by numerical models and experimental results. Finally, Table 2 presents the calibrated heat source parameters. Katayama et al. [37] presented the laser absorption in fiber laser welding of stainless steel, and it was found that the absorption depends on the wavelength and surface roughness, and decreased with an increase in the welding speed. Therefore, the absorption in the case of laser welding AISI 316L is in the range of 0.36–0.55 [38,39]. In this study, a value of 0.5 is used in simulations of V600, and a good correlation of melt pool shape is observed. Therefore, the same value of laser absorption is applied to all the study. The parameter n in Eq. (2) is calibrated automatically by software to ensure the desired value for energy input (625 Watt).

Fig. 7 illustrates numerical and experimental results of the weld pool morphology. The melting temperature is 1400°. First, the measured fusion profile after the manufacturing are presented. The cross-section of melt pool decreases with the increasing of welding speed, as the line energy input decrease (equal to energy input dividing by welding speed). Overall, a good correlation is found between these results. Note that the presented melt pool is observed in the deformed geometry after the manufacturing, including the mechanical deformation. Even though the line energy input decrease, the melt pool length increases with the increasing of welding speed.

Numerical results of temperature evolution are also compared to those given by thermocouples in three points P1, P2, and P3. For simplicity, the $V600$, $V1600$, and $V2600$ are used to represent the results obtained from the welding speed of 600 mm/min, 1600 mm/min, and 2600 mm/min respectively. Fig. 8 shows a perfect correlation between numerical and experimental results. An acceptable maximal relative error less than 5% is found.

The melt pool morphology can be employed to calibrate the heat source model, and the proposed heat source is capable of reproducing almost the same melt pool shape (width, length, depth) as the experiments. In addition, the temperature evolution comparisons between numerical and experimental results checked the whole thermal model's accuracy, including the heat source model, material properties, laser absorptivity, and boundary conditions. Numerical experience shows that the comparisons of temperature evolution and width are indispensable steps to validate the whole thermal model; unfortunately, the measurements of melt

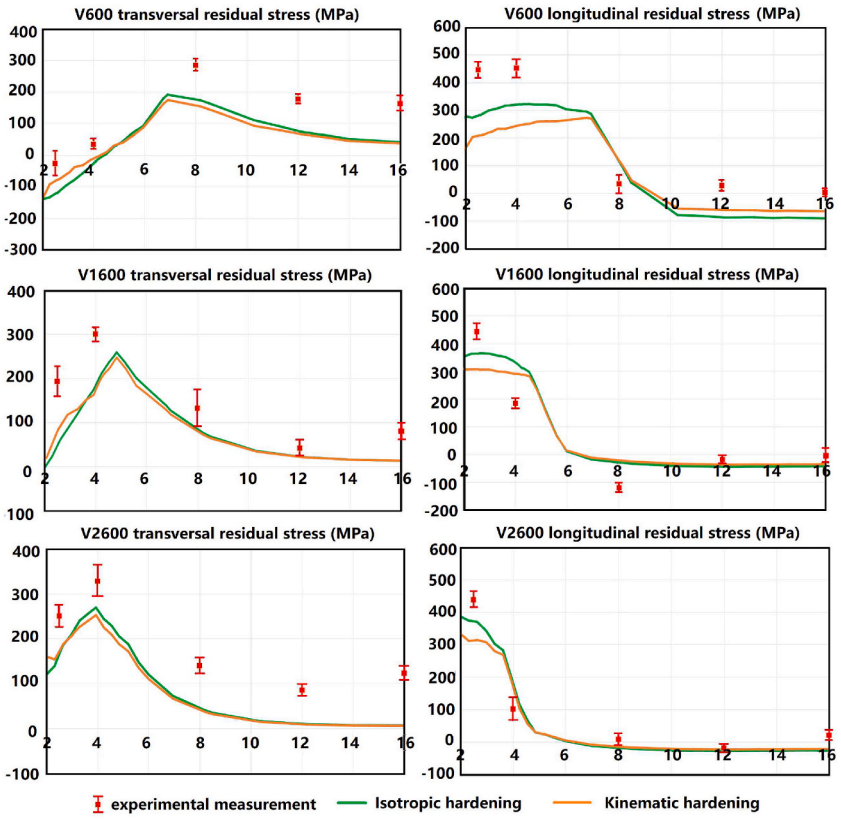

Fig. 9. Comparisons of the transversal and longitudinal residual stresses.

Table 4
Transversal residual stress measured by DRX machine (unit: [MPa]).

	2.5 (mm)	4 (mm)	8 (mm)	12 (mm)	16 (mm)
V600	−25 ± 27	36 ± 39	287 ± 15	179 ± 19	164 ± 14.5
V1600	192 ± 34	300 ± 15	133 ± 42	44 ± 18	81 ± 19
V2600	252 ± 25	330 ± 35	141 ± 18	87 ± 13	124 ± 11

Table 5
Longitudinal residual stress measured by DRX machine (unit: [MPa]).

	2.5 (mm)	4 (mm)	8 (mm)	12 (mm)	16 (mm)
V600	445 ± 28	452 ± 32	33 ± 33	29 ± 19	3 ± 13
V1600	445 ± 28	186 ± 18	−118 ± 16	−19 ± 15	−3 ± 22
V2600	440 ± 20	103 ± 28	10 ± 16	−18 ± 15	21 ± 16

pool width have been rarely reported in the aforementioned experiments. One should notice that if only the comparison of fusion profile (melt pool width and melt pool depth) is performed, nothing ensures that the melt pool length and whole thermal model are accurately predicted. One should note that the inaccurate thermal results will be used for mechanical predictions.

Once the thermal validation has finished, mechanical results of numerical and experimental studies are compared. As first mechanical results, Table 3 provides a comparison of maximal vertical displacements for three welding speeds. It is found that the maximal vertical displacement decrease when the welding speed increase. The kinematic hardening model leads to smaller vertical displacements than those of isotropic hardening. For welding speed of V600, the vertical displacement simulated by kinematic hardening model is closer to experimental values. For the others welding speed, both isotropic and kinematic hardening model give good correlation with measurements.

Fig. 9 shows a comparison between the experimental and numerical results of transversal and longitudinal residual stresses. Experimental results of residual stresses measured at the upper surface of the plate, with a distance 2 mm − 16 mm away from the weld center-line. Tables 4 and 5 provide the measured residual stresses. In general, 16 mm from centre-line of weld bead is far enough to

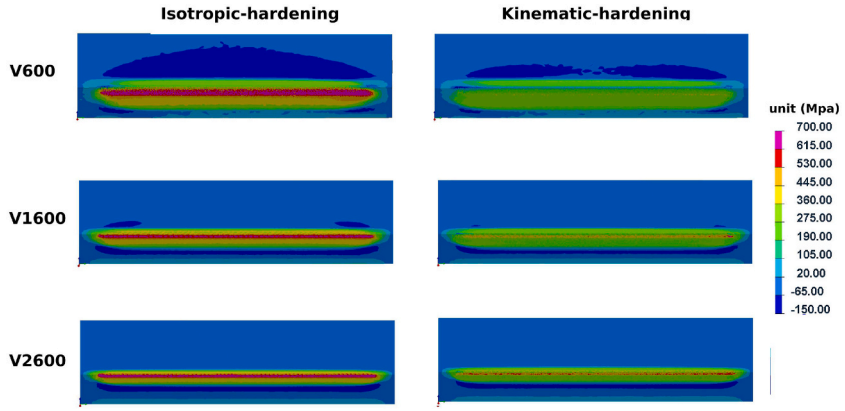

Fig. 10. The distributions of the longitudinal residual stress (σ_{yy}) simulated by different hardening models.

ensure a very small residual stress.

From residual stresses results presented in Fig. 9, several conclusions can be made:

- A significant effect of hardening patterns is noted in the HAZ, where the material has been plasticized and experienced cyclic loading. This effect is less visible outside the HAZ;
- Same tendency of residual stresses can be observed between numerical and experimental results;
- Maximum residual stresses increase when welding speed increases. For example, a difference of 100 MPa is found between the maximal value of the longitudinal residual stress for speeds of 600 mm/min and 2600 mm/min.

Fig. 9 shows the simulated transversal residual stresses by kinematic and isotropic models are comparable, while the longitudinal residual stress are different at the heat-affected zone (HAZ). Fig. 10 provides contours of longitudinal residual stresses for better appreciating the effect of hardening model. Different from the comparison of transversal residual stress, it is found that the hardening model has an important effect on longitudinal residual stresses. Indeed, residual stress values given by the model with an isotropic hardening are clearly much higher than those of the kinematic hardening model at HAZ. This difference can be explained by the fact that the HAZ undergoes strong compression stress (heating phase) and tensile stress (cooling phase) during the process. Thus, Bauschinger effect can strongly decrease tensile yield strength.

5. Conclusion

In this study, a complete experimental benchmark of a laser welding case has been presented. It allowed to have enriched knowledge on different physical quantities for three welding speeds (molten pool morphology, temperature evolution, distortions, and residual stresses). Thermo-mechanical simulations were performed to simulate laser welding process.

The following more specific conclusions can be drawn from this work:

- Variation of welding speed during the experimental study showed that it has a great effect on the molten pool morphology and temperature evolution. For example, the weld pool was shallower and longer for high speeds. It is also found that the increase of this speed leads to an increase in the residual stress, while distortion decrease. These effects of welding speed were also confirmed by numerical simulations.
- A 3D numerical heat source (elliptical truncated conical shape) with Gaussian power density distribution has been defined using experimental thermal results (molten pool morphology and temperature evolution). It is found that this heat source has the capability to accurately reproduce experimental thermal cycles and is able to simulate laser's welding process as closer of real physics.
- It is found that hardening model has an important effect on residual stresses at the HAZ zone. Distortion become less sensible to hardening model with increasing of welding speed.

To better identify the hardening model for laser welding simulation, it would be necessary to carry out the satoh tests. Note that the proposed benchmark can be used by other authors to test or validate different numerical models.

Author statement

Manuscript entitled: *An experimental and numerical case study of thermal and mechanical consequences induced by laser welding process*.

All persons who meet authorship criteria are listed as authors, and all authors certify that they have participated sufficiently in the work to take public responsibility for the content, including participation in the concept, design, analysis, writing, or revision of the manuscript. Furthermore, each author certifies that this material or similar material has not been and will not be submitted to or published in any other publication.

Authorship contributions:

Conceptualization, Y.J., Y.S., J.S., H.H.;
Methodology, Y.J., Y.S., J.S., H.H.;
Software, Y.J., J.-M. B.;
Validation, Y.J., Y.S., H.H., J.-M. B., J.-C.R.;
Writing-original draft preparation, Y.J., Y.S., H.H., J.-C.R.;
Writing-review and editing, Y.J., Y.S., H.H., J.S., J.-C.R., J.-M.B.;
Supervision, J.-M.B.;
Project administration, J.-M.B.;
All authors have read and agreed to the published version of the manuscript.
Signed by all the authors as follows:
Yabo JIA Yassine SAADLAOUI Hédi HAMDI Julien SIJOBERT.
Jean-Christophe ROUX Jean-Michel BERGHEAU.

Declaration of competing interest

The authors declare that they have no known competing financial interests or personal relationships that could have appeared to influence the work reported in this paper.

Acknowledge

Authors are also thankful to Yonggang DUAN (ESI Group) for technical support of this research.

References

[1] Z. Lei, J. Zou, D. Wang, Z. Guo, R. Bai, H. Jiang, C. Yan, Finite-element inverse analysis of residual stress for laser welding based on a contour method, Opt Laser. Technol. 129 (2020), https://doi.org/10.1016/j.optlastec.2020.106289. Article 106289.
[2] Y. Rong, G. Mi, J. Xu, Y. Huang, C. Wang, Laser penetration welding of ship steel EH36: a new heat source and application to predict residual stress considering martensite phase transformation, Mar. Struct. 61 (2018) 256–267, https://doi.org/10.1016/J.MARSTRUC.2018.06.003.
[3] R. Fakir, N. Barka, J. Brousseau, Case study of laser hardening process applied to 4340 steel cylindrical specimens using simulation and experimental validation, Case Stud. Therm. Eng. 11 (2018) 15–25, https://doi.org/10.1016/j.csite.2017.12.002.
[4] P. Ninpetch, P. Kowitwarangkul, S. Mahathanabodee, P. Chalermkarnnon, P. Rattanadecho, Computational investigation of thermal behavior and molten metal flow with moving laser heat source for selective laser melting process, Case Stud. Therm. Eng. 24 (2021), 100860, https://doi.org/10.1016/j.csite.2021.100860.
[5] T. Liu, W. Yan, W. Wu, S. Wang, Thermal performance enhancement of vapor chamber with modified thin screen mesh wick by laser etching, Case Stud. Therm. Eng. 28 (2021), 101525, https://doi.org/10.1016/j.csite.2021.101525.
[6] Y. Rong, T. Lei, J. Xu, Y. Huang, C. Wang, Residual stress modelling in laser welding marine steel EH36 considering a thermodynamics-based solid phase transformation, Int. J. Mech. Sci. 146–147 (2018) 180–190, https://doi.org/10.1016/j.ijmecsci.2018.07.04.
[7] J. Xu, C. Chen, T. Lei, W. Wang, Y. Rong, Inhomogeneous thermal-mechanical analysis of 316L butt joint in laser welding, Opt Laser. Technol. 115 (2019) 71–80, https://doi.org/10.1016/j.optlastec.2019.02.012.
[8] E.D. Derakhshan, N. Yazdian, B. Craft, S. Smith, R. Kovacevic, Numerical simulation and experimental validation of residual stress and welding distortion induced by laser-based welding processes of thin structural steel plates in butt joint configuration, Opt Laser. Technol. 104 (2018) 170–182, https://doi.org/10.1016/j.optlastec.2018.02.026.
[9] K. Devendranath Ramkumar, Sidharth Dev, K.V. Phani Prabhakar, R. Rajendran, K. Giri Mugundan, S. Narayanan, Microstructure and properties of Inconel 718 and AISI 416 laser welded joints, J. Mater. Process. Technol. 266 (2019) 52–62, https://doi.org/10.1016/j.jmatprotec.2018.10.039.
[10] Y. Saadlaoui, J. Sijobert, M. Doubenskaia, P. Bertrand, E. Feulvarch, J.M. Bergheau, Experimental study of thermomechanical processes: laser welding and melting of a powder bed, Crystals 10 (4) (2020) 246, https://doi.org/10.3390/cryst10040246.
[11] F. Cavilha Neto, M. Pereira, L.E.S. Paes, M.R. Viotti, M.C. Fredel, Reducing processing-induced residual stresses in SAE 4140 steels laser welded using modulated power emission, Opt Laser. Technol. 140 (2021), https://doi.org/10.1016/j.optlastec.2021.107032.
[12] L. Li, G. Peng, J. Wang, J. Gong, H. Li, Experimental study on weld formation of Inconel 718 with fiber laser welding under reduced ambient pressure, Vacuum 151 (2018) 140–147, https://doi.org/10.1016/j.vacuum.2018.02.008.
[13] R. Li, T. Wang, C. Wang, F. Yan, X.Y. Shao, X.Y. Hu, J.M. Li, A study of narrow gap laser welding for thick plates using the multi-layer and multi-pass method, Opt Laser. Technol. 64 (2014) 172–183, https://doi.org/10.1016/j.optlastec.2014.04.015.
[14] J. Li, Q. Sun, K. Kang, Z. Zhen, Y. Liu, J. Feng, Process stability and parameters optimization of narrow-gap laser vertical welding with hot wire for thick stainless steel in nuclear power plant, Opt Laser. Technol. 123 (2020), 105921, https://doi.org/10.1016/j.optlastec.2019.105921, 123.
[15] J. Ahn, E. He, L. Chen, T. Pirling, J.P. Dear, C.M. Davies, Determination of residual stresses in fibre laser welded AA2024-T3 T-joints by numerical simulation and neutron diffraction, Mater. Sci. Eng., A 712 (2018) 685–703, https://doi.org/10.1016/j.msea.2017.12.027.
[16] S. Chen, Y. Wu, Y. Li, M. Chen, Q. Zheng, X. Zhan, Study on 2219 Al-Cu alloy T-joint used dual laser beam bilateral synchronous welding: parameters optimization based on the simulation of temperature field and residual stress, Opt Laser. Technol. 132 (2020), 106481, https://doi.org/10.1016/j.optlastec.2020.106481.
[17] P. Duranton, J. Devaux, V. Robin, P. Gilles, J.M. Bergheau, 3D modelling of multipass welding of 316L stainless steel pipe, J. Mater. Process. Technol. 153–154 (2004) 457–463, https://doi.org/10.1016/j.jmatprotec.2004.04.128.
[18] E. Feulvarch, V. Robin, J.M. Bergheau, Thermometallurgical and mechanical modelling of welding – application to multipass dissimilar metal girth welds, Sci. Technol. Weld. Join. 16 (3) (2011) 221–226, https://doi.org/10.1179/1362171811Y.0000000008.
[19] J. Herrnring, P. Staron, N. Kashaev, B. Klusemann, Multiscale process simulation of residual stress fields of laser beam welded precipitation hardened AA6082, Materialia 3 (2018) 243–255, https://doi.org/10.1016/j.mtla.2018.08.010.
[20] H. Huang, S. Tsutsumi, J. Wang, L. Li, H. Murakawa, High performance computation of residual stress and distortion in laser welded 301L stainless sheets, Finite Elem. Anal. Des. 135 (2017) 1–10, https://doi.org/10.1016/j.finel.2017.07.004.
[21] H. Huang, J. Chen, Z. Feng, H.P. Wang, W. Cai, B. Carlson, Large-scale welding process simulation by GPU parallelized computing, Weld. J. 100 (2021) 359–370, https://doi.org/10.29391/2021.100.032.
[22] Y. Saadlaoui, E. Feulvarch, A. Delache, J.-B. Leblond, J.-M. Bergheau, A new strategy for the numerical modeling of a weld pool, Compt. Rendus Mec. 346 (2018) 999–1017, https://doi.org/10.1016/j.crme.2018.08.007.
[23] Z. Zhang, C. Wu, Effect of fluid flow in the weld pool on the numerical simulation accuracy of the thermal field in hybrid welding, J. Manuf. Process. 20 (2015) 215–223, https://doi.org/10.1016/j.jmapro.2015.08.001.
[24] J. Xu, Y. Rong, Y. Huang, P. Wang, C. Wang, Keyhole-induced porosity formation during laser welding, J. Mater. Process. Technol. 252 (2018) 720–727, https://doi.org/10.1016/j.jmatprotec.2017.10.038.

[25] X. Xie, J. Zhou, J. Long, Numerical study on molten pool dynamics and solute distribution in laser deep penetration welding of steel and aluminum, Opt Laser. Technol. 140 (2021), https://doi.org/10.1016/j.optlastec.2021.107085. ISSN 0030-3992.
[26] P. Jiang, S. Gao, S. Geng, C. Han, G. Mi, Multi-physics multi-scale simulation of the solidification process in the molten pool during laser welding of aluminum alloys, Int. J. Heat Mass Tran. 161 (2020), 120316, https://doi.org/10.1016/j.ijheatmasstransfer.2020.120316, 161.
[27] J.-Q. Gao, G.-L. Qin, J.-L. Yang, J.-G. He, T. Zhang, C.-S. Wu, Image processing of weld pool and keyhole in Nd:YAG laser welding of stainless steel based on visual sensing, Trans. Nonferrous Metals Soc. China 21 (2011) 423–428, https://doi.org/10.1016/S1003-6326(11)60731-0.
[28] J.-M. Bergheau, R. Fortunier, Finite Element Simulation of Heat Transfer, John Wiley & Sons, 2013.
[29] A.M. Kamara, W. Wang, S. Marimuthu, L. Li, Modelling of the melt pool geometry in the laser deposition of nickel alloys using the anisotropic enhanced thermal conductivity approach, in: Proceedings of the Institution of Mechanical Engineers, Part B: Journal of Engine. Manuf. vol. 225, 2011, pp. 87–99, https://doi.org/10.1177/09544054JEM2129.
[30] K.H. Lee, G.J. Yun, A novel heat source model for analysis of melt Pool evolution in selective laser melting process, Addit. Manuf. 36 (2020), 101497, https://doi.org/10.1016/j.addma.2020.101497.
[31] Y. Jia, Y. Saadlaoui, J.-M. Bergheau, A temperature-dependent heat source for simulating deep penetration in selective laser melting process, Appl. scien. 11 (2021) 11406, https://doi.org/10.3390/app112311406.
[32] Y. Jia, J.M. Bergheau, J.B. Leblond, J.C. Roux, R. Bouchaoui, S. Gallée, A. Brosse, A new nodal-integration-based finite element method for the numerical simulation of welding processes, Metals 10 (2020) 1386, https://doi.org/10.3390/met10101386.
[33] Y. Jia, J.B. Leblond, J.C. Roux, R. Lacroix, J.M. Bergheau, Applications of a nodal-integration-based finite element method to non-linear problems, in: Proceedings of 14th World Congress on Computational Mechanics (WCCM XIV) SCIPEDIA, 2021, https://doi.org/10.23967/wccm-eccomas.2020.069.
[34] M.C. Smith, A.C. Smith, Advances in weld residual stress prediction: a review of the NeT TG4 simulation round robins part 2, mechanical analyses, Int. J. Pres. Ves. Pip. (2018), https://doi.org/10.1016/j.ijpvp.2018.03.007.
[35] L. Depradeux, J.F. Jullien, Experimental and numerical simulation of thermomechanical phenomena during a Tig welding process, J Phys IV France 120 (2004) 694–704, https://doi.org/10.1051/jp4:2004120080.
[36] Software *SYSWELD*^{TM} Version 21, Reference Analysis Manual, ESI Group Lyon, France, 2019.
[37] S. Katayama, Fundamentals and features of laser welding, in: Fundamentals and Details of Laser Welding. Topics in Mining, Metallurgy and Materials Engineering, Springer, Singapore, 2020, https://doi.org/10.1007/978-981-15-7933-2_3.
[38] J.F. Ready, Industrial Applications of Lasers, second ed., Academic press, New York, 1997.
[39] J. Yan, Y. Zhou, R. Gu, X. Zhang, W.-M. Quach, M. Yan, A comprehensive study of steel powders (316L, H13, P20 and 18Ni300) for their selective laser melting additive manufacturing, Metals 9 (1) (2019) 86, https://doi.org/10.3390/met9010086.

Update

Case Studies in Thermal Engineering
Volume 39, Issue , November 2022, Page

DOI: https://doi.org/10.1016/j.csite.2022.102414

Case Studies in Thermal Engineering 39 (2022) 102414

Contents lists available at ScienceDirect

Case Studies in Thermal Engineering

journal homepage: www.elsevier.com/locate/csite

Corrigendum to "An experimental and numerical case study of thermal and mechanical consequences induced by laser welding process" [Case Stud. Therm. Eng. 35 (2022) 102078]

Yabo Jia *, Yassine Saadlaoui, Hédi Hamdi, Julien Sijobert, Jean-Christophe Roux, Jean-Michel Bergheau

University of Lyon, Ecole Centrale de Lyon-ENISE, LTDS, UMR 5513 CNRS, 58 Rue Jean Parot, 42023, Saint-Etienne Cedex 02, France

The authors regret that some errors were found in their article after publication.
The authors wish that the units indicated in the nomenclature are those used in their study, and also correct some typos:

• C	heat capacity (J kg^{-1} K^{-1})
• Q	heat source per unit volume (W mm^{-3})
• H1, H2	kinematic parameters (MPa)
• Ratio, n	heat source parameter (−)
• Re2, Ri2	heat source parameter (mm)
• δ	Stefan-Boltzmann constant (kg s^{-3} K^{-4})
• h_{con}	convective loss coefficient (W mm^{-2} K^{-1})
• λ_{xx}, λ_{yy}, λ_{zz}	thermal conductivity in X,Y,Z direction (W mm^{-1} K^{-1})
• σ_y	yield stress (MPa)
• Z	coordinate in depth (mm)
• Q_0	normalized maximal energy input per unit volume (W mm^{-3})
• **σ**	Cauchy stress (MPa)
• **S**	fourth-order compliance (MPa)

The two followings should be removed:

• q_{heat}	input heat flux (W)
• q_{loss}	heat losses (W)

Eq. 1 should be corrected as follows:

$$\rho C\frac{\partial T}{\partial t}=\frac{\partial}{\partial x}\left(\lambda_{xx}\frac{\partial T}{\partial x}\right)+\frac{\partial}{\partial y}\left(\lambda_{yy}\frac{\partial T}{\partial y}\right)+\frac{\partial}{\partial z}\left(\lambda_{zz}\frac{\partial T}{\partial z}\right)+Q$$

Neumann condition : $\lambda grad\, T\cdot\mathbf{n} = q(T,\ t)$ on $\partial\Omega_q$

DOI of original article: https://doi.org/10.1016/j.csite.2022.102078.
* Corresponding author.
E-mail address: yabo.jia@enise.fr (Y. Jia).

https://doi.org/10.1016/j.csite.2022.102414

Available online 7 September 2022

Dirichlet condition: $T = T_p(t)$ on $\partial\Omega_T$

$$\partial\Omega = \partial\Omega_q + \partial\Omega_T$$

where ρ and C are, respectively, the density and specific heat. λ_{xx}, λ_{yy}, λ_{zz} represent the thermal conductivity of X,Y,Z directions. T is the temperature. $\partial\Omega$ is the boundary of domain Ω. Q represents internal heat source per unit volume. q and T_p are prescribed heat flux and temperature on the boundary.

The correct form of Eq. 2 is:

$$Q = n^{*}Q_0{*}\exp\left(-\frac{X^2}{a^2} \ -\frac{Y^2}{b^2}\right)$$

$$b = \frac{Z - z_i}{z_e - z_i} * (Re2 - Ri2) + Ri2$$

$$a = \frac{b}{Ratio}$$

The texts below Eq. 5 must be corrected as follows:

The global strain $\boldsymbol{\varepsilon} = \frac{1}{2}(\mathbf{grad}\ \vec{u} + \mathbf{grad}^{\mathbf{T}}\ \vec{u})$ is associated to the displacement field $\vec{u}$. This global strain can be decomposed as an elastic part $\boldsymbol{\varepsilon^e}$, a (visco)plastic part $\boldsymbol{\varepsilon^p}$, and a thermal part $\boldsymbol{\varepsilon^T}$.

Elastic strain, $\boldsymbol{\varepsilon^e}$, is a function of the stress tensor $\boldsymbol{\sigma}$, and can be expressed as:

$$\boldsymbol{\varepsilon^e} = \boldsymbol{S} : \boldsymbol{\sigma}$$

where **S** is the fourth-order compliance tensor defined by elastic coefficients.

The authors would like to apologise for any inconvenience caused.